OPEN ACCESS



Reionization with SIMBA: How Much Does Astrophysics Matter in Modeling Cosmic Reionization?

Sultan Hassan^{1,2}, Romeel Davé^{2,3,4}, Matthew McQuinn⁵, Rachel S. Somerville¹, Laura C. Keating⁶, Daniel Anglés-Alcázar^{1,7}, Francisco Villaescusa-Navarro^{1,8}, and David N. Spergel^{1,8}, Daniel Anglés-Alcázar^{1,7}, Francisco Villaescusa-Navarro^{1,8}, and David N. Spergel^{1,8}, Daniel Astrophysics, Flatiron Institute, 162 5th Avenue, New York, NY 10010, USA; shassan@flatironinstitute.org Department of Physics & Astronomy, University of the Western Cape, Cape Town 7535, South Africa Institute for Astronomy, University of Edinburgh, Royal Observatory, Edinburgh EH9 3HJ, UK

4 South African Astronomical Observatories, Observatory, Cape Town 7925, South Africa

5 Department of Astronomy, University of Washington, Seattle, WA 98195, USA

6 Leibniz-Institute for Astrophysics Potsdam (AIP), An der Sternwarte 16, D-14482 Potsdam, Germany
7 Department of Physics, University of Connecticut, 196 Auditorium Road, U-3046, Storrs, CT 06269, USA
8 Department of Astrophysical Sciences, Princeton University, Peyton Hall, Princeton, NJ 08544, USA

Received 2021 August 21; revised 2022 April 2; accepted 2022 April 22; published 2022 May 25

Abstract

Traditional large-scale models of reionization usually employ simple deterministic relations between halo mass and luminosity to predict how reionization proceeds. We here examine the impact on modeling reionization of using more detailed models for the ionizing sources as identified within the $100\ h^{-1}$ Mpc cosmological hydrodynamic simulation SIMBA, coupled with postprocessed radiative transfer. Comparing with simple (one-to-one) models, the main difference with using SIMBA sources is the scatter in the relation between dark matter halos and star formation, and hence ionizing emissivity. We find that, at the power spectrum level, the ionization morphology remains mostly unchanged, regardless of the variability in the number of sources or escape fraction. In particular, the power spectrum shape remains unaffected and its amplitude changes slightly by less than 5%–10%, throughout reionization, depending on the scale and neutral fraction. Our results show that simplified models of ionizing sources remain viable to efficiently model the structure of reionization on cosmological scales, although the precise progress of reionization requires accounting for the scatter induced by astrophysical effects.

Unified Astronomy Thesaurus concepts: Reionization (1383); Galaxy evolution (594); Radiative transfer simulations (1967)

1. Introduction

Many upcoming surveys, such as the Square Kilometer Array (SKA; Mellema et al. 2013), the Hydrogen Epoch of Reionization Array (HERA; DeBoer et al. 2017), the Low Frequency Array (LOFAR; van Haarlem et al. 2013), are devoted to detecting reionization in the near future via its impact on H I 21 cm emission topology. On the other hand, the James Webb Space Telescope (JWST; Gardner et al. 2006), the Vera C. Rubin Observatory Legacy Survey of Space and Time (LSST; Ivezić et al. 2019), and Nancy Grace Roman Space Telescope (Roman; Spergel et al. 2015), are devoted to detecting the primary sources driving reionization at high redshift (galaxies and quasars). With these growing observational efforts, we are moving toward an era of detailed observations of high-redshift galaxy formation. It is therefore important to test and quantify the uncertainties in our current models of reionization, by exploring the interplay between galaxy formation and cosmology, in order to prepare for extracting the maximum amount of information from future surveys.

The main sources of uncertainties in reionization models arise from the ionizing source population (Stark 2016), the clumpiness of the ionized gas (which sets the number of recombinations; D'Aloisio et al. 2020), and approximations in

Original content from this work may be used under the terms of the Creative Commons Attribution 4.0 licence. Any further distribution of this work must maintain attribution to the author(s) and the title of the work, journal citation and DOI.

performing the radiation transport (RT) (Wu et al. 2021). The impact of RT has been investigated in detail in several studies (e.g., Mesinger et al. 2011; Zahn et al. 2011; Majumdar et al. 2014; Molaro et al. 2019), which found that, using the same ionizing sources, the Excursion-Set Formalism (Press & Schechter 1974; Bond et al. 1991), which is an algorithm to identify maximally ionized bubbles within spherical regions around sources, produces similar topology to the postprocessing radiative transfer of cosmological hydrodynamic simulations. Hence, it appears justified to use excursion-set-based models to study the reionization signal on large scales. Meanwhile, the impact of including inhomogeneous recombination and clumping effects—the sink model—has also been studied in several works (e.g., Sobacchi & Mesinger 2014; Hassan et al. 2016), which concluded that inhomogeneous recombination reduces the ionized region size, delays reionization, and suppresses the large-scale 21 cm power. In contrast, the large-scale impact of including more physically motivated recipes to model the ionizing source population has not been studied. This is the goal of this work.

In Hassan et al. (2016), we took a first step to study the impact of modeling ionizing sources more accurately within seminumerical simulations and showed that including power-law mass-dependent ionizing emissivity motivated from hydrodynamical simulations as opposed to the usual linear dependence on mass (through an efficiency parameter $\zeta \equiv R_{\rm ion}/M_{\rm h}$ of ionizing photon emissivity $R_{\rm ion}$ versus halo mass $M_{\rm h}$) increases the duration of reionization and boosts the small-scale 21 cm power spectrum. This indicates that a modest change in the ionizing emissivity—halo mass $(R_{\rm ion}-M_{\rm h})$ relation

has a major impact on reionization globally. This impact owes to the more massive sources in the superlinear scaling being more clustered and hence producing larger H II regions (Furlanetto et al. 2006; McQuinn et al. 2007).

Currently, the most accurate way to model ionizing sources in a cosmological volume is through state-of-the-art cosmological hydrodynamical galaxy formation simulations, in which star formation is modeled following, for instance, the subgrid multiphase model of Springel & Hernquist (2003) or the H₂-regulated model of Krumholz et al. (2009). Such simulations include ILLUSTRIS (Genel et 2014), ILLUSTRISTNG (Pillepich et al. 2018), EAGLE (Schaye et al. 2015), Horizon-AGN (Kaviraj et al. 2017), SIMBA (Davé et al. 2019), Cosmic Reionization on Computers (CROC; Gnedin 2014; Gnedin & Kaurov 2014), Cosmic Dawn II (CoDA II; Ocvirk et al. 2020), SPHINX (Katz et al. 2021), and THESAN (Kannan et al. 2022) using the AREPO-RT (Kannan et al. 2019), to name a few. It has recently become possible to run galaxy formation simulations on cosmological scales $(\gtrsim 100 \,\mathrm{Mpc})$ while resolving halos down to $M_{\rm h} < 10^{10} \,M_{\odot}$, thanks to advances in computing capabilities. Hence, it is now possible to ask the question: Does detailed astrophysics matter for modeling cosmic reionization?

The main difference in using sources identified within these galaxy formation simulations consists of including the scatter around the $R_{\rm ion}$ – $M_{\rm h}$ relation. This scatter, which is due to stellar feedback, merger history, and/or photon escape fraction, might have a direct correlation with the density field and/or other properties, such as metallicity, and hence its impact on large-scale reionization remains nontrivial. As a simple example, by assuming a log-normal scatter around sources identified within seminumerical excursion-set-based models, Whitler et al. (2020) showed that the scatter reduces the Ly α visibility for the brightest galaxies.

In this work, we use ionizing sources identified within the state-of-the-art SIMBA simulation, which has been shown to reproduce a wide range of observations, at both low z (see Davé et al. 2019) and during the reionization epoch (Leung et al. 2020; Wu et al. 2020). We consider a broad range of source models that uses the SIMBA star formation rates (SFRs) as inputs but considers different spatial distributions and varied escape fraction pictures. We then run large-scale radiative transfer reionization simulations, with the radiative transfer done in postprocessing using ATON (Aubert & Teyssier 2008, 2010) via a moment-based method with an M1 closure relation. We compare these results with a simple power-law model of the ionizing emissivity as a function of halo mass, as commonly used in large-scale seminumerical models. Compared to previous works (e.g., Whitler et al. 2020), our approach has several advantages and improvements, namely the scatter in ionization rate naturally emerges from the detailed subgrid physics implemented within SIMBA, and the impact on large-scale topology is determined through accurate modeling of radiative transfer with ATON.

This paper is organized as follows: We briefly describe the SIMBA simulation in Section 2.1, introduce the source models in Section 2.2, explain how the reionization realization is generated in Section 2.3, present our results in Section 3, and conclude in Section 4. Throughout this work, we adopt a Λ CDM cosmology with parameters $\Omega_m = 0.3$, $\Omega_{\Lambda} = 0.7$, $\Omega_b = 0.048$, h = 0.68, $\sigma_8 = 0.82$, and $n_s = 0.97$, consistent

with Planck Collaboration et al. (2016) constraints. All quantities are in comoving units unless otherwise noted.

2. Methods

2.1. SIMBA Simulations

We here briefly describe SIMBA and refer the reader to Davé et al. (2019) for more detailed information about the physics implemented in the simulation.

The SIMBA model was introduced in Davé et al. (2019). SIMBA is a follow-up to the MUFASA (Davé et al. 2016) cosmological galaxy formation simulation using GIZMO's meshless finite-mass hydrodynamics solver (Hopkins 2015, 2017). Radiative cooling and photoionization heating are implemented using the updated GRACKLE-3.1 library (Smith et al. 2017). A spatially uniform ionizing background from Haardt & Madau (2012) is assumed, in which self-shielding is accounted for following Rahmati et al. (2013). The chemical enrichment model tracks nine elements (C, N, O, Ne, Mg, Si, S, Ca, and Fe) arising from Type II supernovae (SNe), Type Ia SNe, and asymptotic giant branch (AGB) stars. Type Ia SNe and AGB wind heating are also included. The star-formation-driven galactic winds are kinetically launched and decoupled into hot- and cold-phase winds, and the winds are metal loaded owing to local enrichment from SNe, with the overall metal mass being conserved. The mass rate entering galactic outflows is modeled with a broken power law following Anglés-Alcázar et al. (2017b). The quasi-linear scaling of wind velocity with escape velocity from Muratov et al. (2015) is adopted. SIMBA further implements black hole growth via a torque-limited accretion model (Anglés-Alcázar et al. 2017a), and the feedback from active galactic nuclei (AGNs) is implemented in both radiative and jet modes. SIMBA also accounts for the X-ray AGN feedback in the surrounding gas following Choi et al. (2012). Dust production and destruction are modeled on the fly, leading to predictions of dust abundance that broadly agree with a variety of constraints over cosmic time (Li et al. 2019).

SIMBA employs a molecular-gas-based prescription following Krumholz et al. (2009, hereafter KMT) to form stars. KMT is a physically motivated recipe to model star formation as seen in local disk galaxies, where a strong correlation is seen between SFR and molecular-gas content (e.g., Leroy et al. 2008). Star formation is only allowed in the dense gas phase (ISM gas) above a hydrogen number density $n_{\rm H} \geqslant 0.13~{\rm cm}^{-3}$, though in practice the H₂ fraction forces star formation to occur at much higher densities ($n_{\rm H} \gg 1~{\rm cm}^{-3}$). SIMBA assumes a Chabrier (2003) initial mass function (IMF) throughout.

SIMBA is an attractive platform to use in this study due to its ability to match a wide range of observations as shown in Davé et al. (2019). These observations include the stellar-massfunction evolution, main sequence, evolution in gas fractions (both neutral and molecular), the gas-phase and stellar-massmetallicity relations, galaxy photometric projected sizes, hot halo gas fractions, black-hole-mass-stellar-mass relation, and the dust-mass function. On the other hand, SIMBA fails to produce a sharp knee in the stellar-mass function at z=0 and produces larger low-mass quenched galaxy sizes, to name a few examples. Despite these small disagreements, SIMBA remains a state-of-the-art platform for studying the scatter impact on reionization morphology.

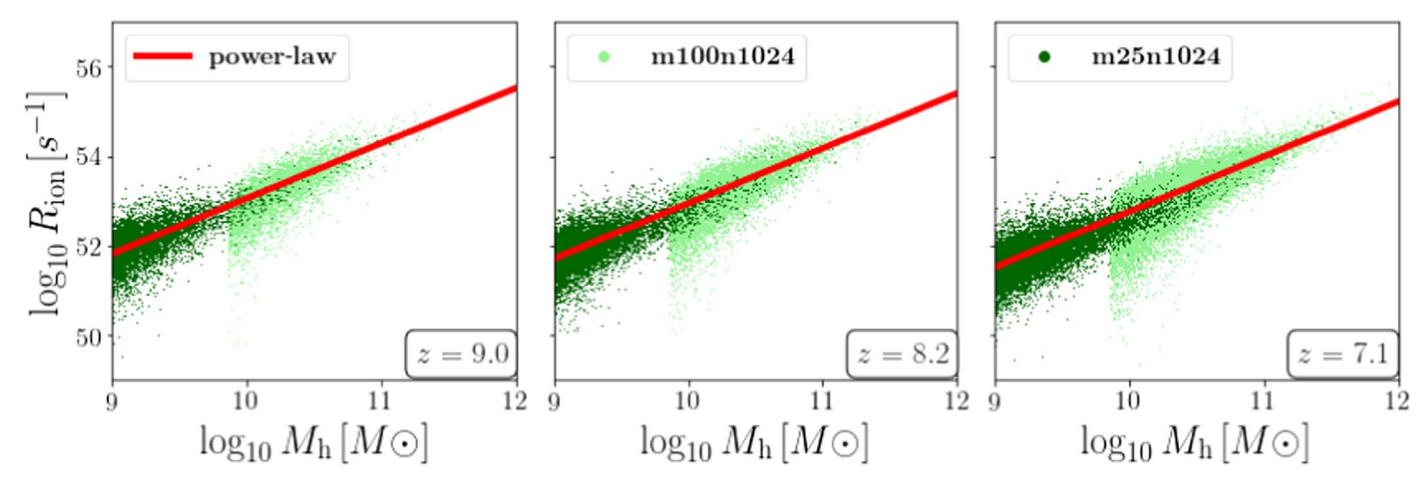


Figure 1. Ionization rate R_{ion} as a function of halo mass M_h from resolved halos at different redshifts in the fiducial (m100n1024, light green) and high-resolution (m25n1024, dark green) SIMBA runs using Equation (2). The red line represents the fitting functions (from Equation (3)), which we will use later to study the scatter impact.

2.2. Source Models

The ionization rate $(R_{\rm ion})$ from each galaxy is computed using a stellar-metallicity-dependent parameterization of the ionizing photon flux (Q(Z)), which reproduces the equilibrium values compiled by Schaerer (2003). This Q(Z) parameterization is provided by Finlator et al. (2011):

$$\log_{10} Q(Z) = 0.639(-\log_{10} Z)^{1/3} + 52.62 - 0.182, \quad (1)$$

where Q is in units of $s^{-1}(M_{\odot} \text{ yr}^{-1})^{-1}$ and the last term converts to a Chabrier (2003) IMF. It is straightforward to convert the Q to R_{ion} using the SFR as follows:

$$R_{\rm ion} = Q \times SFR.$$
 (2)

We directly compute the ionizing emissivity from the SIMBA halo catalogs. We use the stellar-mass-weighted metallicity Z of all star particles and the total SFR of all gas particles within each halo to evaluate Equation (2) in order to provide the emissivity required for the radiative transfer calculations.

As mentioned earlier, our aim is to use these realistic sources, as identified within SIMBA, to study the impact on reionization on cosmological scales, as compared to simplified models. We use the largest SIMBA run available, which has a volume of $100 \ h^{-1}$ Mpc with 1024^3 dark matter and gas particles each. While this simulation has a sufficiently large volume suitable to study large-scale reionization (Iliev et al. 2014), the dark matter particle mass resolution is about $9.6 \times 10^7 \ M_{\odot}$, and hence the minimum halo mass resolved would be of order $10^9 M_{\odot}$ assuming 16 particles as the minimum to identify halos in the friends-of-friends finder. However, if the resolution is high enough to resolve low-mass halos down to $10^8 M_{\odot}$, the number of sources increases, and in this case the scatter impact would be even smaller because the ionizing emissivity average in pixels is now taken over a larger number of sources. Later we include models with different numbers of sources to address this point.

To construct a simple model of the average $R_{\rm ion}$ as a function of halo mass—a comparison model that averages out the fluctuations of individual halos—we follow our earlier approach presented in Hassan et al. (2016), where we obtained a parameterization for the ionizing emissivity $R_{\rm ion}$ as a function of halo mass $M_{\rm h}$ and redshift z from hydrodynamic simulations.

We here repeat the same exercise to obtain the best-fitting parameters for the following simple model of R_{ion} :

$$R_{\rm ion}/M_{\rm h} = A(1+z)^D (M_{\rm h}/B)^C \exp(-(B/M_{\rm h})^3),$$
 (3)

where A, B, C, and D are free parameters. This fitting function, which is similar to the Schechter function, is motivated by the fact the $R_{\rm ion}$ behaves as a power-law at high halo masses and exhibits a turnover at the low-mass end. In Hassan et al. (2016), we found the turnover occurs around $10^8 M_{\odot}$ (see Figure 1 therein). Because the largest SIMBA run used in this study resolves halos down to $\sim 10^9 - 10^{10} M_{\odot}$, we refer to models using this simple relation (Equation (3)) as "power law."

In order to estimate the slope of R_{ion} more accurately from SIMBA, we include a higher-resolution run, which has a smaller volume of 25 h^{-1} Mpc with the same number of particles (2×1024^3) . Hence, this run resolves halos down to $10^{8.5} M_{\odot}$; halos below this mass are not expected to contribute significantly (Finlator et al. 2011). We combine these two simulations at different redshifts (z = 6-10) to obtain the R_{ion} best-fitting parameters as shown in Figure 1. Conservatively, one may obtain the best-fit parameters using catalogs from high (e.g., z = 20) to low (e.g., z = 6) redshifts. However, restricting the fitting to redshifts lower than z = 10 would not impact the results since reionization, in models considered in this study, begins only afterward. This figure shows R_{ion} as a function of M_h at different z from SIMBA m100n1024 (light green) and m25n1024 (dark green) runs using Equation (2). The fitting function, Equation (3), is shown in red, and the best-fitting parameters are found using a nonlinear least-squares fit as $A = 3.51 \times 10^{39} \pm 5.6 \times 10^{37} [s^{-1}],$ $B = 3.3 \times 10^8 \pm 2.6 \times 10^6$ [M_{\odot}], $C = 0.234 \pm 0.00078$, and $D = 3.2 \pm 0.0082$. These parameters are similar to those found earlier by Hassan et al. (2016), based on full radiative hydrodynamic simulations (with a much smaller volume). It is evident that these parameters produce a good fit to the ionizing emissivity at different redshifts, and hence we will use this fit as our power-law model of R_{ion} to compare with using a more realistic R_{ion} directly from SIMBA.

To perform a consistent comparison and to carefully investigate the scatter impact, we tune the photon escape fraction so that all models would produce roughly the same number of ionizing photons. In addition, we ensure that all

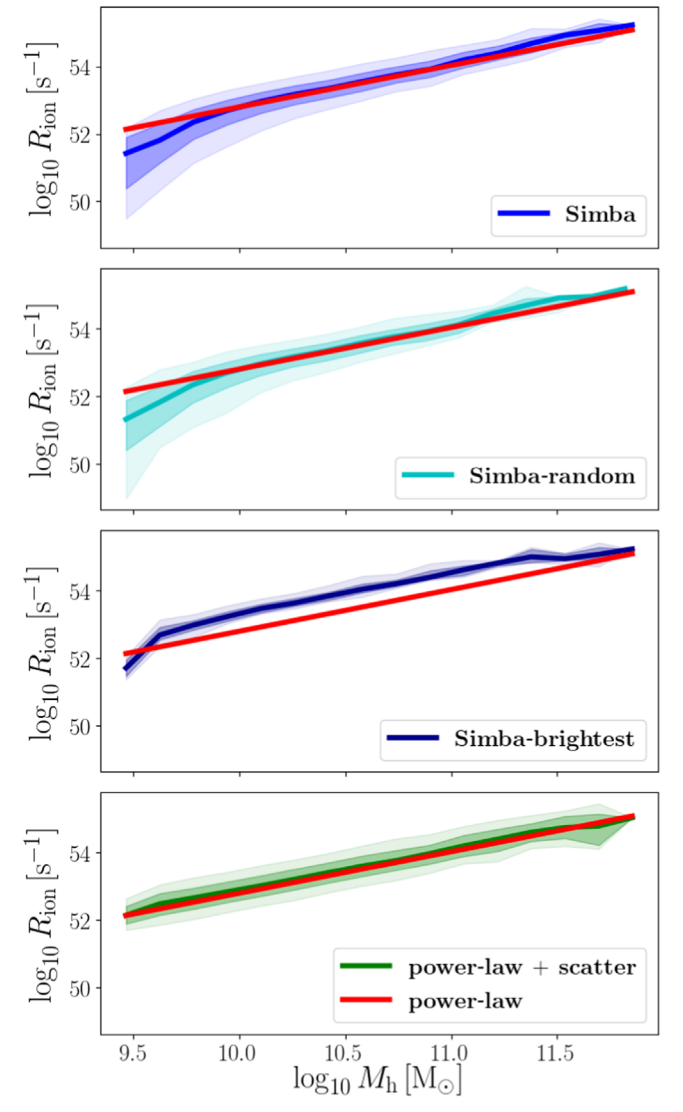


Figure 2. Ionization rate $R_{\rm ion}$ as a function of halo mass at $z \sim 7$ for the different source models considered in this study. The top three panels show different SIMBA variants, and the bottom panel shows the power-law model with/without scatter. In all panels, we show the power law in red. Solid lines represent the 50th percentile of the different $R_{\rm ion}$ distributions, and the dark and light shaded areas are the corresponding $1\sigma-2\sigma$ levels, respectively.

models do produce the expected ionizing emissivity evolution (e.g., Becker & Bolton 2013) as well as the neutral fraction measurements by the end of reionization (e.g., Fan et al. 2006; Bouwens et al. 2015). It is worth noting that, for the purpose of this study, it is not important to match or reproduce any measurements. The most important part of this analysis is to ensure that the comparison is performed at the same redshift and neutral fraction in order to exclude any other cosmological and astrophysical effects.

Using the same density field and recombination rate, we consider five different source models that are tuned to emit a similar amount of ionizing photons and obtain the same reionization history as follows:

- 1. *Simba*: uses all sources with emissivities computed using Equation (2) and $f_{\rm esc} = 0.25$ (blue in Figure 2).
- 2. Simba-random: uses only 25% of all sources, randomly selected within different halo mass bins of 0.25 dex.

- Similar to Simba, the emissivity is computed using Equation (2), but with $f_{\rm esc} = 1.0$ (cyan in Figure 2).
- 3. *Simba-brightest*: uses only the brightest halos (the most luminous halos) in each mass bin of 0.25 dex (halos with the highest $R_{\rm ion}$). These halos are about 7% of all halos. Similar to Simba-random in terms of emissivity and unity $f_{\rm esc}$ (dark blue in Figure 2).
- 4. *Power law*: uses all sources with emissivities computed using Equation (3), and $f_{\rm esc} = 0.25$ (red line in Figure 2).
- 5. Power law with scatter: Same as power law, except with the addition of a scatter assuming that $R_{\rm ion}$ may be represented by a log-normal distribution with a mean given by Equation (3) and standard deviation set to 0.3 dex.⁹ This model uses $f_{\rm esc} = 0.2$ (green in Figure 2).

A visual summary of these different models is provided in Figure 2, where solid lines represent the 50th percentile of the different R_{ion} distributions, and the dark and light shaded areas are the corresponding 1σ – 2σ levels, respectively. As a reference, we show in red the power-law model in all panels. All these models include different sources of scatter. For instance, the scatter in the Simba-random and Simba-brightest models is based on the variability of the photon escape fraction and considers an extreme case where some halos (whether randomly or the brightest) have $f_{\rm esc} = 1$ and the rest are completely obscured ($f_{\rm esc} = 0$). Simba-brightest is motivated by the fact that galaxies with high SFR would have stronger feedback (more gas ejection) and hence higher $f_{\rm esc}$. The other models, Simba or power law with scatter, include different forms of scatter either from SIMBA's detailed subgrid physics or by assuming a simple log-normal distribution, respectively while assuming the same $f_{\rm esc}$. It is worth noting that the Simba and power-law models are found to obtain the same reionization history using the same photon escape fraction of 25%. This shows that the power-law model is a good representative of the average $R_{\rm ion}$ in SIMBA. In fact, the power law approximately represents the average of all considered models, except Simba-brightest, where the models differ by a factor of 2–3. This shows that comparisons with these different models would reveal the impact of variability within either the number of sources or $f_{\rm esc}$. While the scatter in SIMBA increases the total $R_{\rm ion}$ by $\sim 20\%$ at the massive end, this increase has a negligible effect on the reionization history because the number density of massive sources ($> 10^{11} M_{\odot}$) is small as compared to the faint ones. In addition, it is also seen in the top panel of Figure 2 that the power law has a higher R_{ion} slope at the lowmass end than the average in SIMBA (blue solid line), which boosts the total R_{ion} in the power-law model to a similar level to SIMBA. By contrast, the power law with scatter requires a 20% lower $f_{\rm esc}$ compared to the power law. This is a consequence of assuming that the Rion can be modeled using a log-normal distribution, where the median is somewhat less than the mean. This shows that $f_{\rm esc}$ is highly sensitive to the assumptions used to build the source model. We compare all these models in terms of their large-scale ionization morphology in Section 3.

2.3. Radiative Transfer

All reionization realizations from different source models are obtained in postprocessing using the radiative transfer module ATON (Aubert & Teyssier 2008, 2010), which is a moment-

 $^{^{9}}$ This amount of scatter (0.3 dex) is the average scatter over the full halo mass range as measured in SIMBA.

based method with an M1 closure relation. We run reionization from $z \sim 20$ down to $z \sim 5$, using all snapshots available in this redshift range, which are about 35 snapshots in the time interval of about 20 Myr. Single frequency has been used, and temperature has been evolved. We assume a blackbody spectrum with temperature $T = 5 \times 10^4 K (E = 20.27 \text{ eV})$ and full speed of light (c = 1). A similar version of ATON has been used in e.g., Keating et al. (2020) and Kulkarni et al. (2019), for instance, to study the large-scale opacity fluctuations and Ly α forest by the end of reionization. The main difference in our analysis lies in considering different source models as explained in the previous section. We first smooth densities of gas particles on a grid with a number of cells $N = 256^3$, resulting in a resolution of 390.625 ckpc h^{-1} . While this is a somewhat coarse density grid, in Hassan et al. (2016), we have performed a convergence test using the same source model R_{ion} for different resolutions and configurations and found that the change in the power spectrum remains minimal. Hence, we do not expect the number of cells would alter the conclusion. Using the gas density grids with the ionizing emissivities as inputs, we use ATON to self-consistently compute the ionization field, gas temperature, and the photoionization rate. We run ATON with all source models, and compare the results in the following section.

3. Results: Reionization Morphology

We here compare the effect of using the different source models described in the previous sections on reionization morphology. The main difference between these models lies in the scatter in the $R_{\rm ion}$ – $M_{\rm h}$ relation, and hence this study shows the impact of including different forms of scatter on reionization.

In Figures 3 and 4, we show a comparison between all models in terms of maps of the ionization field and their corresponding power spectra at different redshifts, respectively. We can see that the morphology remains mostly unaffected as seen in the maps, as well as the power spectra. This is also seen in the ratio between all models to the power-law model (bottom panels in Figure 4), which is close to unity in all cases. However, it is expected for the Simba-random and Simbabrightest models to have lower small-scale power, due to the smaller number of sources compared to other models. This effect is clearly seen at the early stages of reionization where bubbles are small. As reionization proceeds and bubbles grow, all models seem to have the same power ratio, except for the Simba-brightest model, due to the difference in the global neutral fraction. In addition, the source clustering and bias only change in the Simba-brightest model, which is the reason for its higher large-scale power compared to other models, particularly at the late stages of reionization. All of these effects are too small to cause noticeable differences in the maps. It is worth mentioning that we have also checked the opposite scenario to the Simba-brightest model, where only the faintest halos are used with unity $f_{\rm esc}$. In that case (i.e., Simba-faintest), nearly 50% of halos are required to yield similar emissivity and reionization history to other models. All results remain unchanged whether random, brightest, or faintest halos are used. This minimal impact might be due to the fact that hundreds, if not thousands, of galaxies exist within large ionized bubbles and hence the scatter would average out. In this case, the scatter impact would be reduced by a factor of $\sim 1/\sqrt{N}$, where N is the number of sources. Because these

comparisons are performed at the same redshift and the 21 cm brightness temperature field traces the ionization topology, the same conclusion is valid for the 21 cm fluctuations on large scales. This shows that including different forms of scatter in the $R_{\rm ion}$ – $M_{\rm h}$ relation has a minimal impact on reionization morphology. However, we have checked the bispectra between these models and found bigger differences (scatter induces a more negative bispectrum, hence larger skewness). We leave the investigation of the impact of scatter on higher-order summary statistics to future works.

4. Conclusions

We have studied the impact of scatter on reionization morphology by considering a broad range of models with different variations in the photon escape fractions and emissivities, using sources identified within the state-of-the-art galaxy formation simulation SIMBA. The main improvement over previous works is the inclusion of a realistic scatter in the R_{ion} – M_{h} relation. The radiative transfer is performed using the ATON routine, which implements a moment-based method with an M1 closure relation. We postprocess the radiative transfer on SIMBA's largest available simulation run, which has a comoving volume of $100 \, h^{-1}$ Mpc, sufficient to yield convergent reionization histories and capture the bubble overlap epoch by the end of reionization (Iliev et al. 2014).

Besides models with a scatter, we constructed a simple source model (power-law) using a fitting function (Equation (3)) that behaves as a power law for halos larger than SIMBA's resolution limit (>10 $^9\,M_\odot$). This model adopts a one-to-one $R_{\rm ion}$ – $M_{\rm h}$ relation. We show in Appendix A that those missing halos below $10^9\,M_\odot$ do not change the reionization morphology but are important to accurately estimate the ionization history and astrophysical parameters such as the photon escape fraction.

To investigate the impact of the scatter, we tune the number of sources and photon escape fractions in all models to produce similar evolution in the comoving ionizing emissivity density and reionization history. Our main key finding can be summarized as follows: The scatter in the $R_{\rm ion}$ – $M_{\rm h}$ relation does not significantly alter the reionization morphology as seen in the ionization maps (see Figure 3) or the power spectra (see Figure 4) if computed at the same global ionization fraction.

It is worthwhile to mention several limitations associated with this work. The radiative transfer is modeled using a moment-based method with an M1 closure that is known to overionize Lyman-limit systems in post-reionization and does not accurately capture shadowing (e.g., Wu et al. 2021). The radiative transfer also has been run in postprocessing and hence these results do not include the coupling between the hydrodynamics and radiative transfer. We also do not account for contribution from binary stars that would induce earlier reionization (e.g., Rosdahl et al. 2018; Doughty & Finlator 2021). Additionally, due to the low resolution in the current SIMBA run, we have relaxed the requirement to identify dark matter halos, assuming only 16 particles as a minimum to capture smaller halos. While we have checked explicitly that the results remain the same when we require a larger number of dark matter particles (e.g., 64) to identify halos, the comparison between Simba-random and Simba-brightest with Simba, where a smaller number of sources was used (e.g., 25% and 7%), provides evidence that, irrespective of the number of sources, models (with/without scatter) at approximately the

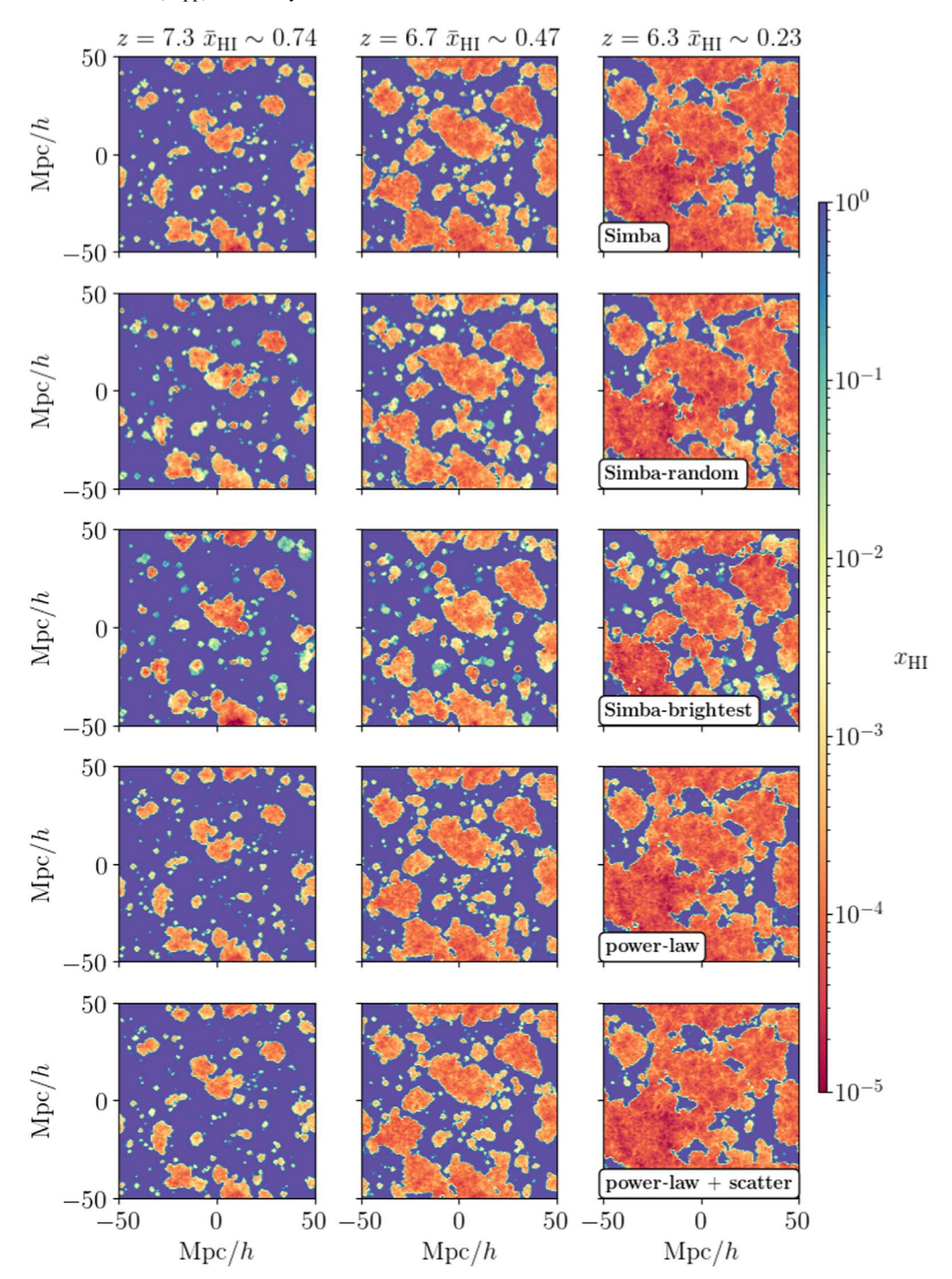


Figure 3. Comparison between ionization maps for all models, at different redshifts and stages during reionization. All models produce similar maps, indicating that the scatter, either in the ionizing emissivity (SIMBA vs. power-law models) or in the photon escape fractions (comparing all SIMBA variants), has a minimal impact on the large-scale morphology.

same neutral fraction would produce similar reionization morphology on cosmological scales. Recent works (e.g., Ma et al. 2020; Ocvirk et al. 2021) have shown that the photon escape fraction depends on halo mass and varies by \sim 2 orders of magnitude between low- and high-mass halos. Although most of our models adopt a constant $f_{\rm esc}$, Simba-brightest adopts an extreme case in $f_{\rm esc}$ variability, where 7% of all halos (the brightest) are given unity $f_{\rm esc}$ and the rest (93%) have $f_{\rm esc}=0$. This implies that, regardless of $f_{\rm esc}$ variability with halo mass, the reionization morphology remains relatively similar (comparing Simba-brightest to other models). In Appendix B,

we attempt to gain deeper insights into the minimal impact of scatter on the large-scale morphology by comparing the ionizing emissivity history for randomly selected halos in terms of the dark matter halo evolution versus the star formation history.

Iyer et al. (2020) have performed a detailed comparison between different galaxy formation models (Illustris, IllustrisTNG, Mufasa, Simba, and EAGLE) and found that the variability of star formation histories within these simulations broadly show a similar power spectral density that is well described by a broken power law. This indicates that similar

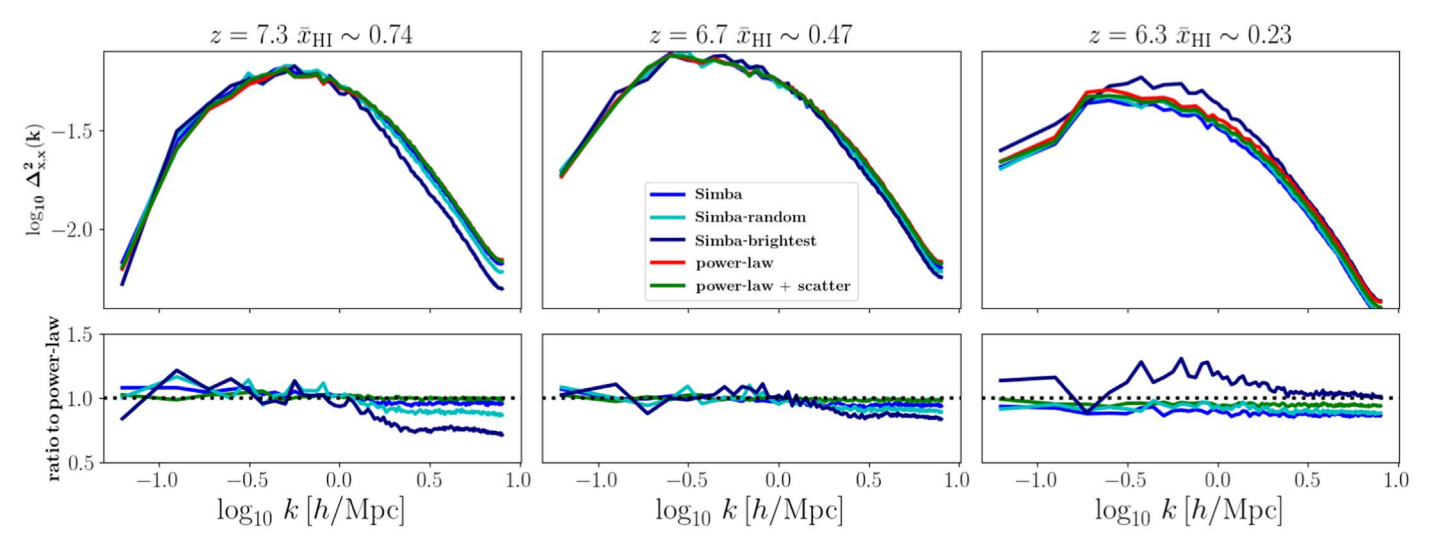


Figure 4. Comparison between ionization power spectra for all models, at different redshifts and stages during reionization (top panels). The bottom panels show the power ratio of all models to the power-law model. As seen in Figure 3, all models produce similar power spectra on small and large scales, irrespective of the variability in the emissivity or in the photon escape fraction.

results would be obtained using any of these galaxy formation models because the R_{ion} history follows closely the SF history. In addition, most radiative transfer hydrodynamic simulations use either the OTVET or M1 approximation to solve the moment-based radiative transfer equation, which has been shown to perform similarly during the early and intermediate stages of reionization but overionize self-shielding absorbers by the same amount by end of reionization (see, e.g., Wu et al. 2021). This suggests that regardless of the radiative transfer method, the similar conclusion might be drawn. As seen in Figure 1, the scatter decreases toward higher masses, which can be resolved within larger box sizes. Because the massive halos are very rare, we do not expect their presence to have a significant impact on the results but a slight modification to $f_{\rm esc}$ might be required to obtain the same reionization history. It is worth mentioning that the scatter would increase the number of sources above a specific luminosity threshold, and hence future surveys with JWST will be able to place tighter constraints on the scatter. We leave performing detailed JWST forecasting using SIMBA to future works.

Our results suggest that simplified models of ionizing sources, with some calibration of the parameters such as the photon escape fraction, can be used as a viable computationally efficient tool to model reionization on cosmological scales.

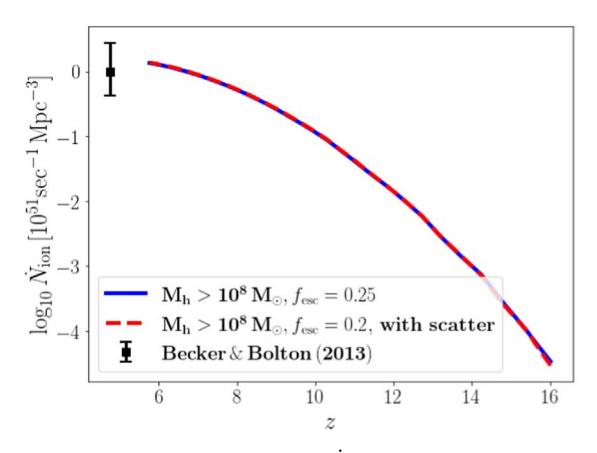
The authors acknowledge helpful discussions with Adam Lidz and Enrico Garaldi. We thank Dominique Aubert for providing ATON and Jonathan Chardin for guidance on how to use it. We thank the anonymous referee for constructive comments, which have improved the manuscript significantly. S.H. and R.S.S. acknowledge support from the Simons Foundation. R.D. acknowledges support from the Wolfson Research Merit Award program of the U.K. Royal Society. D. A.A. acknowledges support by NSF grant AST-2009687. F.V. N. acknowledges funding from the WFIRST program through NNG26PJ30C and NNN12AA01C. L.C.K. was supported by the European Union's Horizon 2020 research and innovation program under Marie Skłodowska-Curie grant agreement No. 885990. SIMBA was run using the DiRAC@Durham facility managed by the Institute for Computational Cosmology on behalf of the U.K. STFC DiRAC HPC Facility. The equipment was funded by BEIS capital funding via STFC capital grants ST/P002293/1, ST/R002371/1, and ST/S002502/1; Durham University; and STFC operations grant ST/R000832/1.

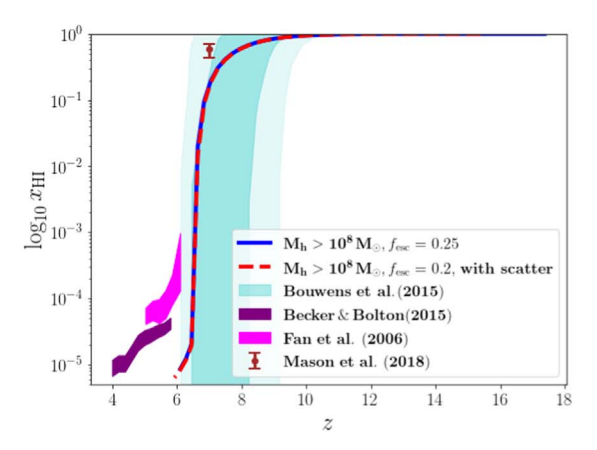
Appendix A Contribution of Halos $<10^9 M_{\odot}$

Because our results are based on the SIMBA simulation, which does not resolve halos below $<10^9 M_{\odot}$, we here aim to quantify whether these halos are expected to change the reionization signal on cosmological scales. For this test, we make use of a seminumerical approach, SIMFAST21 (Santos et al. 2010). We use the same cosmology, volume, and number of cells to generate the density field grids and halos using SIMFAST21. We set the minimum halo mass in the excursionset formalism to $M_h = 10^8 M_{\odot}$. We then consider the powerlaw model with/without scatter to run ATON with the whole population of halos above $>10^8 M_{\odot}$ and compare results in Figure 5. We compare these two runs in terms of the reionization topology at relatively the same ionized fraction and redshift. We find that the topology remains unaffected as seen in the ionization maps and in the corresponding ionization power. This indicates that the results presented in the main text remain valid, irrespective of these missing halos ($<10^9 M_{\odot}$).

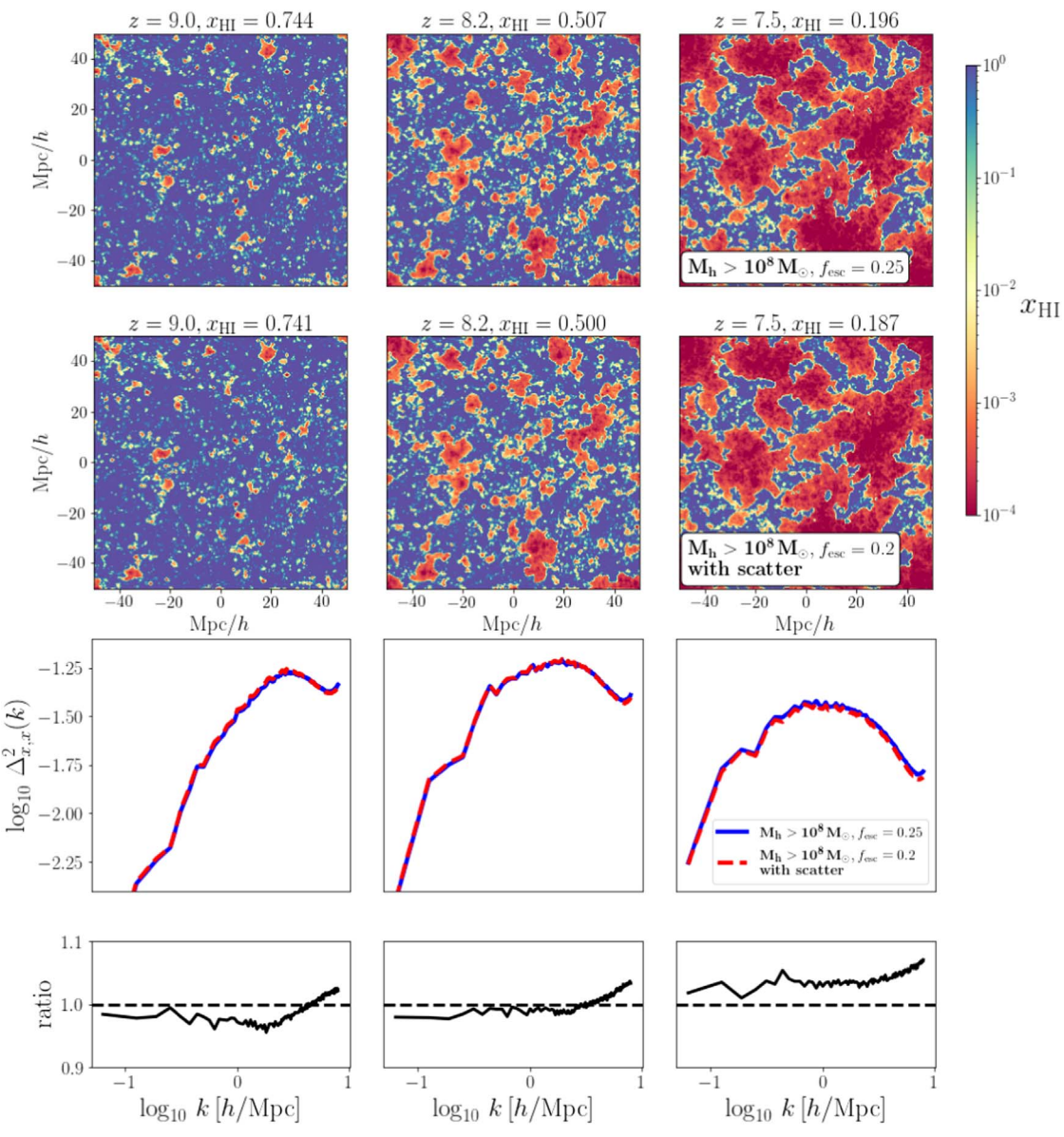
Appendix B Variability in R_{ion} History

To gain deeper insights into the scatter impact due to the evolution in dark matter or SF, we here focus on the variability in $R_{\rm ion}$ history for individual halos as shown in Figure 6. We first compute the $R_{\rm ion}$ history (solid lines) from SIMBA using the star formation history, which is a measure of the total star formation occurring over a time interval (Δt) , and the metallicity history, which quantifies the mass-weighted metallicity over Δt . We use the ages, masses, and metallicities of all stellar particles associated with halos to compute these histories with $\Delta t = 10$ Myr, and the $R_{\rm ion}$ history is then computed using Equation (2). We next compute the $R_{\rm ion}$ history differently in terms of the dark matter evolution over time (dashed lines), in which we trace halos back in time to identify their progenitors and use their masses and redshifts in the power-law formula





- (a) Ionizing emissivity density, $\dot{N}_{\rm ion},$ evolution as a function of redshift.
- (b) Reionization history as compared with various measurements.



(c) Ionization maps and power spectra at different redshifts.

Figure 5. Test with SIMFAST21 to examine the contribution of halos with $M_h < 10^9 M_{\odot}$ that are missing in SIMBA due to resolution. This figure indicates that those halos have no impact on the large-scale morphology.

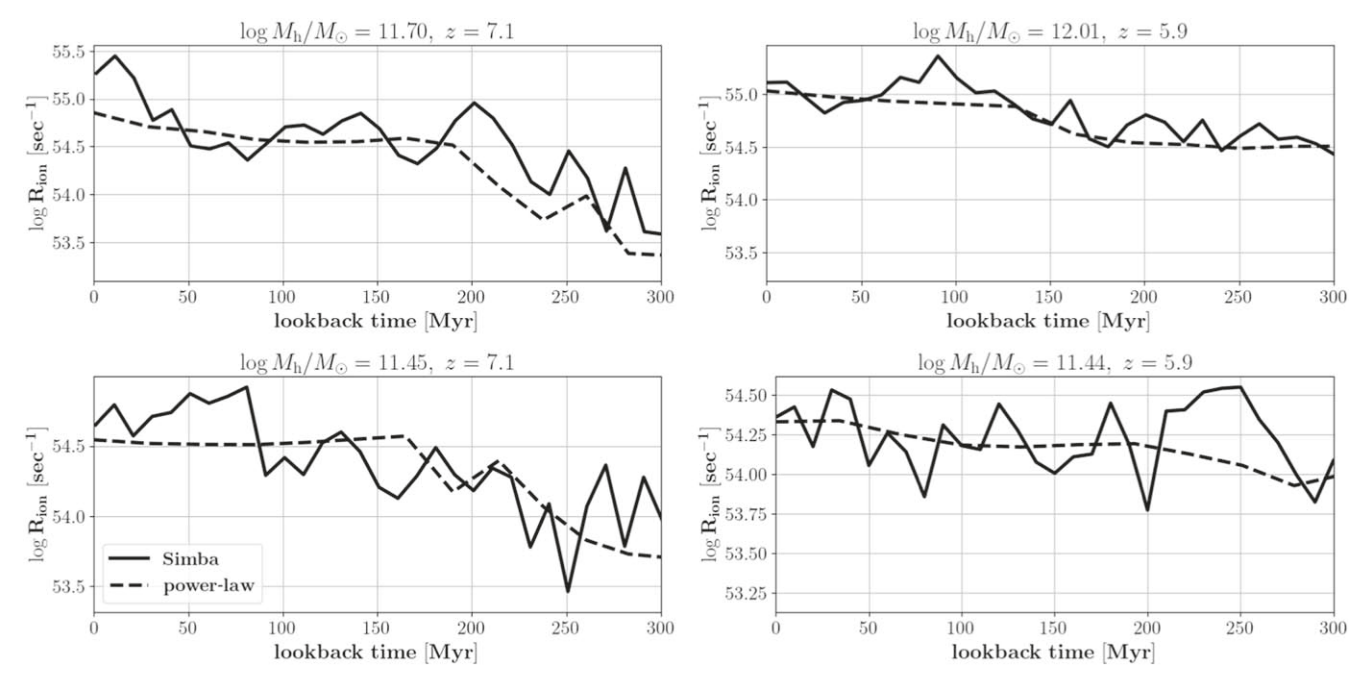


Figure 6. Examples of the $\log_{10} R_{\text{ion}}$ history for randomly selected halos as a function of lookback time using the star formation history (SIMBA, solid) and the R_{ion} -fitting formula (power law, dashed) in 10 Myr intervals. Halo masses and redshifts are quoted in the figure legends above the individual panels. The redshift quoted above represents the zero-point in the x-axis. The value of R_{ion} in SIMBA varies by $\lesssim 1$ order of magnitude over time. The smooth evolution in the power-law model, which traces the evolution in dark matter halo mass, is a good approximation to the average R_{ion} evolution in SIMBA. In all cases, the difference in instantaneous R_{ion} between these two models is minimal, and hence similar amounts of photons are emitted. This figure provides insights into why the impact of star formation variability on the global reionization signal is found to be minimal.

(Equation (3)) to compute the R_{ion} . We compare these different forms of $R_{\rm ion}$ histories in Figure 6 for randomly selected halos and quote their masses and redshift in the figure legend. The R_{ion} from SIMBA (solid), which traces the star formation history, fluctuates by $\lesssim 1$ order of magnitude over intervals of 10 Myr. On the other hand, the smooth evolution in the powerlaw model, which traces the evolution in dark matter (dashed lines), is a good approximation of the average R_{ion} evolution in SIMBA. In all cases, the difference in the instantaneous R_{ion} between these different R_{ion} histories is small, and hence similar amounts of photons are emitted in each R_{ion} model. If we instead use a larger bin size in time (e.g., $\Delta t = 30$ or 40 Myr), then the star formation history becomes smoother and similar to the dark matter evolution as seen in the power-law model. This indicates that the scatter might have a minimal impact on the large-scale reionization signal because the average of R_{ion} over time is approximately similar to the smooth evolution of R_{ion} as computed from the evolution in dark matter. This exercise provides insights into why the impact of star formation variability on the global reionization signal is found to be minimal.

ORCID iDs

Francisco Villaescusa-Navarro https://orcid.org/0000-0002-4816-0455

David N. Spergel https://orcid.org/0000-0002-5151-0006

References

Anglés-Alcázar, D., Davé, R., Faucher-Giguère, C.-A., Özel, F., & Hopkins, P. F. 2017a, MNRAS, 464, 2840 Anglés-Alcázar, D., Faucher-Giguère, C.-A., Kereš, D., et al. 2017b, MNRAS, 470, 4698 Aubert, D., & Teyssier, R. 2008, MNRAS, 387, 295 Aubert, D., & Teyssier, R. 2010, ApJ, 724, 244 Becker, G. D., & Bolton, J. S. 2013, MNRAS, 436, 1023 Bond, J. R., Cole, S., Efstathiou, G., & Kaiser, N. 1991, ApJ, 379, 440 Bouwens, R. J., Illingworth, G. D., Oesch, P. A., et al. 2015, ApJ, 811, 140 Chabrier, G. 2003, PASP, 115, 763 Choi, E., Ostriker, J. P., Naab, T., & Johansson, P. H. 2012, ApJ, 754, 125 D'Aloisio, A., McQuinn, M., Trac, H., Cain, C., & Mesinger, A. 2020, ApJ, Davé, R., Anglés-Alcázar, D., Narayanan, D., et al. 2019, MNRAS, 486, 2827 Davé, R., Thompson, R., & Hopkins, P. F. 2016, MNRAS, 462, 3265 DeBoer, D. R., Parsons, A. R., Aguirre, J. E., et al. 2017, PASP, 129, 045001 Doughty, C., & Finlator, K. 2021, MNRAS, 505, 2207 Fan, X., Strauss, M. A., Becker, R. H., et al. 2006, AJ, 132, 117 Finlator, K., Davé, R., & Özel, F. 2011, ApJ, 743, 169 Furlanetto, S. R., McQuinn, M., & Hernquist, L. 2006, MNRAS, 365, 115 Gardner, J. P., Mather, J. C., Clampin, M., et al. 2006, SSRv, 123, 485 Genel, S., Vogelsberger, M., Springel, V., et al. 2014, MNRAS, 445, 175 Gnedin, N. Y. 2014, ApJ, 793, 29 Gnedin, N. Y., & Kaurov, A. A. 2014, ApJ, 793, 30 Haardt, F., & Madau, P. 2012, ApJ, 746, 125 Hassan, S., Davé, R., Finlator, K., & Santos, M. G. 2016, MNRAS, 457, 1550 Hopkins, P. F. 2015, MNRAS, 450, 53 Hopkins, P. F. 2017, arXiv:1712.01294 Iliev, I. T., Mellema, G., Ahn, K., et al. 2014, MNRAS, 439, 725 Iyer, K. G., Tacchella, S., Genel, S., et al. 2020, MNRAS, 498, 430 Ivezić, Ž., Kahn, S. M., Tyson, J. A., et al. 2019, ApJ, 873, 111 Kannan, R., Garaldi, E., Smith, A., et al. 2022, MNRAS, 511, 4005 Kannan, R., Vogelsberger, M., Marinacci, F., et al. 2019, MNRAS, 485, 117 Katz, H., Martin-Alvarez, S., Rosdahl, J., et al. 2021, MNRAS, 507, 1254 Kaviraj, S., Laigle, C., Kimm, T., et al. 2017, MNRAS, 467, 4739 Keating, L. C., Weinberger, L. H., Kulkarni, G., et al. 2020, MNRAS, 491, 1736 Krumholz, M. R., McKee, C. F., & Tumlinson, J. 2009, ApJ, 693, 216 Kulkarni, G., Keating, L. C., Haehnelt, M. G., et al. 2019, MNRAS, 485, L24

```
Leroy, A. K., Walter, F., Brinks, E., et al. 2008, AJ, 136, 2782
Leung, T. K. D., Olsen, K. P., Somerville, R. S., et al. 2020, ApJ, 905, 102
Li, Q., Narayanan, D., & Davé, R. 2019, MNRAS, 490, 1425
Ma, X., Quataert, E., Wetzel, A., et al. 2020, MNRAS, 498, 2001
Majumdar, S., Mellema, G., Datta, K. K., et al. 2014, MNRAS, 443, 2843
McQuinn, M., Lidz, A., Zahn, O., et al. 2007, MNRAS, 377, 1043
Mellema, G., Koopmans, L. V. E., Abdalla, F. A., et al. 2013, ExA, 36, 235
Mesinger, A., Furlanetto, S., & Cen, R. 2011, MNRAS, 411, 955
Molaro, M., Davé, R., Hassan, S., Santos, M. G., & Finlator, K. 2019,
   MNRAS, 489, 5594
Muratov, A. L., Kereš, D., Faucher-Giguère, C.-A., et al. 2015, MNRAS,
  454, 2691
Ocvirk, P., Aubert, D., Sorce, J. G., et al. 2020, MNRAS, 496, 4087
Ocvirk, P., Lewis, J. S. W., Gillet, N., et al. 2021, MNRAS, 507, 6108
Pillepich, A., Springel, V., Nelson, D., et al. 2018, MNRAS, 473, 4077
Planck Collaboration, Ade, P. A. R., Aghanim, N., et al. 2016, A&A, 594, A13
Press, W. H., & Schechter, P. 1974, ApJ, 187, 425
```

```
Rahmati, A., Pawlik, A. H., Raicevic, M., & Schaye, J. 2013, MNRAS,
  430, 2427
Rosdahl, J., Katz, H., Blaizot, J., et al. 2018, MNRAS, 479, 994
Santos, M. G., Ferramacho, L., Silva, M. B., Amblard, A., & Cooray, A. 2010,
  MNRAS, 406, 2421
Schaerer, D. 2003, A&A, 397, 527
Schaye, J., Crain, R. A., Bower, R. G., et al. 2015, MNRAS, 446, 521
Smith, B. D., Bryan, G. L., Glover, S. C. O., et al. 2017, MNRAS, 466, 2217
Sobacchi, E., & Mesinger, A. 2014, MNRAS, 440, 1662
Spergel, D., Gehrels, N., Baltay, C., et al. 2015, arXiv:1503.03757
Springel, V., & Hernquist, L. 2003, MNRAS, 339, 289
Stark, D. P. 2016, ARA&A, 54, 761
van Haarlem, M. P., Wise, M. W., Gunst, A. W., et al. 2013, A&A, 556, A2
Whitler, L. R., Mason, C. A., Ren, K., et al. 2020, MNRAS, 495, 3602
Wu, X., Davé, R., Tacchella, S., & Lotz, J. 2020, MNRAS, 494, 5636
Wu, X., McQuinn, M., & Eisenstein, D. 2021, JCAP, 2021, 042
Zahn, O., Mesinger, A., McQuinn, M., et al. 2011, MNRAS, 414, 727
```